

The thermodynamic structure and large-scale structure filament in MACS J0717.5+3745

J. P. Breuer^{1,2*}, N. Werner¹, F. Mernier^{3,4,5}, K. Umetsu⁶, A. Simionescu^{7,8,9}, M. Devlin¹⁰, L. Di Mascolo^{11,12}, T. Dibblee-Barkman¹³, S. Dicker¹⁰, B. S. Mason¹⁴, T. Mroczkowski¹⁵, C. Romero¹⁶, C. L. Sarazin¹⁷, and J. Sievers¹³

¹ Department of Theoretical Physics and Astrophysics, Masaryk University. Kotlářská 2, Brno, 611 37, Czech Republic

² Department of Physics, Graduate School of Advanced Science and Engineering, Hiroshima University Kagamiyama, 1-3-1 Higashi-Hiroshima, 739-8526, Japan

³ NASA Goddard Space Flight Center, Code 662, Greenbelt, MD 20771, USA

⁴ Department of Astronomy, University of Maryland, College Park, MD 20742-2421, USA

⁵ ESA/ESTEC, Keplerlaan 1, 2201 AZ Noordwijk, The Netherlands

⁶ Academia Sinica Institute of Astronomy and Astrophysics (ASIAA), No. 1, Section 4, Roosevelt Road, Taipei 106216, Taiwan

⁷ SRON Netherlands Institute for Space Research, Niels Bohrweg 4, 2333CA Leiden, The Netherlands

⁸ Leiden Observatory, Leiden University, PO Box 9513, 2300 RA Leiden, The Netherlands

⁹ Kavli Institute for the Physics and Mathematics of the Universe (WPI), The University of Tokyo, Kashiwa, Chiba 277-8583, Japan

¹⁰ University of Pennsylvania, 209 S. 33rd St., Philadelphia, PA 19014, USA

¹¹ Kapteyn Astronomical Institute, University of Groningen, Landleven 12, 9747 AD, Groningen, The Netherlands

¹² Laboratoire Lagrange, Université Côte d'Azur, Observatoire de la Côte d'Azur, CNRS, Blvd de l'Observatoire, CS 34229, 06304 Nice cedex 4, France

¹³ Department of Physics, McGill University, 3600 University Street Montreal, QC, H3A 2T8, Canada

¹⁴ National Radio Astronomy Observatory, 520 Edgemont Rd., Charlottesville VA 22903, USA

¹⁵ European Southern Observatory, Karl-Schwarzschild-Straße 2, 85748 Garching bei München, Germany

¹⁶ Center for Astrophysics, Harvard & Smithsonian, 60 Garden Street, Cambridge, MA 02138, USA

¹⁷ Department of Astronomy, University of Virginia, P.O. Box 400325, Charlottesville, VA 22904, USA

Accepted XXX. Received YYY; in original form ZZZ

ABSTRACT

We present the results of Chandra and XMM-Newton X-ray imaging and spatially-resolved spectroscopy, as well as new MUSTANG2 90 GHz observations of the thermal Sunyaev-Zeldovich from MACS J0717.5+3745, an intermediate redshift ($z = 0.5458$) and exceptionally massive ($3.5 \pm 0.6 \times 10^{15} M_{\odot}$) Frontier Fields cluster experiencing multiple mergers and hosting an apparent X-ray bright large scale structure filament. Thermodynamical maps are produced from Chandra, XMM-Newton, and ROSAT data using a new method for modelling the astrophysical and instrumental backgrounds. The temperature peak of 24 ± 4 keV is also the pressure peak of the cluster and closely correlates spatially with the Sunyaev-Zeldovich peaks from the MUSTANG2 data. The cluster center hosts shock fronts to the north and south, for which we report lower limits for the shock Mach numbers of $\mathcal{M} = 1.6 \pm 0.4$ and $\mathcal{M} = 1.9 \pm 0.3$, respectively. Bayesian X-ray Analysis methods were used to disentangle different projected spectral signatures for the filament structure, with Akaike and Bayes criteria being used to select the most appropriate model to describe the various temperature components. We report an X-ray filament temperature of $2.9^{+0.5}_{-0.3}$ keV and a density $(1.60 \pm 0.05) \times 10^{-4} \text{ cm}^{-3}$, corresponding to an overdensity of 150 relative to the critical density of the Universe. We estimate the hot gas mass of the filament to be $\sim 4.4 \times 10^{12} M_{\odot}$, while its total projected weak lensing measured mass is $\sim 6.8 \pm 2.7 \times 10^{13} M_{\odot}$, indicating a hot baryon fraction of 4–10%.

Key words. galaxies: clusters: individual: MACS J0717.5+3745 – galaxies: clusters: intracluster medium – X-rays: galaxies: clusters

1. Introduction

Current cosmological models and numerical simulations predict that the majority of the missing baryons in our Universe sit in the faint galaxy cluster outskirts and the interconnecting filaments of the cosmic web (Cen & Ostriker 1999; Davé et al. 2001). This warm-hot intergalactic medium (WHIM) contributes to the growth of galaxy clusters through a slow constant accretion, as the in-falling filamentary gas virializes within the gravitational potential wells of massive clusters.

Only a small number of X-ray bridges and filaments have been studied so far. This is partially because the diffuse WHIM remains a complicated challenge to detect with today's instruments. Numerical cosmological simulations predict WHIM temperatures of 10^5 to 10^7 K and densities of 10^{-7} to 10^{-4} cm^{-3} (Cen & Ostriker 2006; Haider et al. 2016); in other words, features in the WHIM are inherently characterized by soft X-ray emission, low surface brightness, and poor signal to noise ratios due to dominant contributions to the signal from both astrophysical and instrumental backgrounds. Needless to say, much care needs to be taken when modelling the spectra of these complex regions to

* E-mail: jeanpaul.breuer@gmail.com

account for all of the different contributions from other emission signatures.

Current observational information about filaments is derived from either absorption or emission. Observations in emission have so far been limited to a small number of systems, MACS J0717.5+3745 (Ebeling et al. 2004), Abell 399/401 (Sakelliou & Ponman 2004), Abell 222/223 (Werner et al. 2008), Abell 2811 (+offset)/2804/2801 (Sato et al. 2010), Abell 3558/3556 (Mitsuishi et al. 2012), Abell 2744 (Eckert et al. 2015a), Abell 3391/3395 (Alvarez et al. 2018; Reiprich et al. 2021; Veronica et al. 2022, 2024), Abell 2029/2033 (Mirakhor et al. 2022), and Abell 3667/3651 (Dietl et al. 2024). Temperature measurements were obtained only for four of these systems. For two of the four, it has been reported that the filament emission is dominated by the emission of the Intracluster Medium (ICM), as evidenced by the excessively large temperatures.

There is a debate about the origin of these X-ray filaments. While some of the detected bridges could indeed be classified as WHIM filaments, others are due to other physical processes, such as shock-related compression heating between the two merging atmospheres or emission of ram-pressure stripped tails from in-falling haloes.

One of the most extensively studied merging galaxy clusters in almost every available wavelength is MACS J0717.5+3745 (RA 07h17m32.1, DEC +37°45'21"), an extremely massive, intermediate redshift ($z = 0.5458$), Hubble Frontier Fields Cluster (Ebeling et al. 2001). MACS J0717.5+3745 is also one of the most complex galaxy clusters to date, having hosted at least four different sub-cluster collisions. The collective mass from the many ingested dark matter halos makes this a great target for gravitational lensing studies and additional exploration of local substructures via the Sunyaev-Zeldovich effect due to the high temperatures. The complex mergers have also resulted in a complex ICM morphology, characterized by perturbed plasma discontinuities, stripped atmospheres, shock fronts, and cold fronts, and results in many peculiar features in the X-ray morphology and radio surface brightness features. Besides the gravitational lensing study, Jauzac et al. (2018), also looked at many of these X-ray substructures in detail. Most intriguing is the prominent X-ray bridge located in the S-SE of the cluster, which has previously been studied by van Weeren et al. (2016, 2017) using Chandra data.

This paper aims to investigate the X-ray bridge in detail, statistically disentangling the diverse distribution of complex emission signatures associated with the filament using Bayesian X-ray Analysis (BXA) methods and nested models, along with a new dynamically-adaptive method for the full instrumental background modelling of each region for both Chandra and XMM-Newton. This paper also presents new thermodynamical maps using a joint modelling method combining available data from Chandra, XMM-Newton, and ROSAT, as well as trend-modeled residual maps where the average cluster thermodynamical properties over radial distances are removed. This paper additionally presents previously unpublished data from 90 GHz MUSTANG2 observations of the Sunyaev-Zeldovich effect in the direction of MACS J0717.5+3745. In Section 2, we explain the methods used in the data reduction, followed by Sec. 3 that explains the instrumental and X-ray background model and analysis of both Chandra and XMM-Newton. Section 4 then describes the main results of the thermodynamic maps and the properties of the filament, while Section 5 discusses these results. Throughout the paper, we assume the standard Λ cold dark matter cosmology with $\Omega_m = 0.286$, $\Omega_\Lambda = 0.714$, and $H_0 = 69.6$. Consequently, at $z = 0.5458$, 1 arcmin corresponds to 387.42 kpc. The Wilms

abundance table is adopted for all plasma emission and photoelectric absorption models in the discussed spectral models (Wilms et al. 2000). Unless stated otherwise, the error bars correspond to a 68% confidence interval.

2. Observations and Data Reduction

2.1. Chandra Observations

The data from four *Chandra* pointings (see Tab. 1) were reprocessed using `repro` from the level-1 event lists with the standard software packages using the most recent versions of CIAO and CALDB (versions 4.16 and 4.11.0). The good time intervals (GTI) of the observations after filtering periods of flaring are summarized in Tab. 1. Totalling all available *Chandra* observations gives approximately 228.9 ks of observing time; however, only 211.8 ks were used for creating the data products due to the remaining exposures having experienced flaring contamination which could bias the spectral analysis. All observations were used for creating the surface brightness images; however, only observations 4200, 16235, and 16305 were considered in further spectral analysis as they contained the largest GTIs. Because of the low signal-to-noise ratio, blank-sky background files were explicitly not used in favour of using epoch-specific stowed background files normalized by the data over background count ratio in the 10-12 keV energy range. When dealing with extremely faint X-ray substructures, the stowed background files give additional control over the systematics in the background. Merged broadband images were produced in the 0.5 to 7 keV band, shown in Fig. 1 (left). Unless otherwise specified, the spectra of all regions were extracted from each *Chandra* observation using the `specextract` routine from the latest version of CIAO (version 4.16.0).

2.2. XMM-Newton Observations

Complementary to the *Chandra* data, we also retrieved archival XMM-Newton observations of MACS J0717.5+3745, as listed in Tab. 1. Three pointings showing sufficient data quality were downloaded and reduced using both the XMM Science Analysis System (SAS) software (v20.0.0) and the current calibration files (CCF) by following the procedure detailed in the Extended Source Analysis Software (ESAS v20.0.0) cookbook. To get cleaned event files for each detector, we used the standard `emchain` and `mos-filter` routines on the MOS data, and the `epchain` and `pn-filter` routines on the pn data, which removes periods of anomalously high count rate by calculating GTIs through the `espfilt` routine. The total GTI for each observation are also shown in Tab. 1.

Images were extracted for each detector of each observation using the ESAS tasks `mos-spectra` and `pn-spectra`, while background images were created using the ESAS tasks `mos_back` and `pn_back`, before being combined using the `comb` routine. Point sources were detected using a wavelet detection algorithm, `wavdetect`, by first making a `psfmap` for XMM-Newton with a constant size of 9 arcsec. This is based on the estimate that at 1.5 keV, the $1-\sigma$ integrated volume of a 2D Gaussian for each pixel ranges from 7 arcseconds on-axis to around 11 arcseconds at edge of the FOV, and our selected box region of interest is near the central pointing. Merged broadband images from all observations were produced in the 0.5 to 7 keV band using the `merge_comp_xmm` routine, shown in Fig. 1 (right). A zoomed-in, over-saturated view of the cluster center and filamentary structure (with pointsources removed) can be seen in Fig. 2.

Table 1. Summary of the data, excluding overly contaminated observations. GTI is the net exposure good time intervals for all instruments after cleaning the data. (*) Not used.

Telescope	ObsID	Date	GTI (ks)
<i>Chandra</i>	1655(*)	2001-01-29	17.1
<i>Chandra</i>	4200	2003-01-08	57.2
<i>Chandra</i>	16235	2013-12-13	67.9
<i>Chandra</i>	16305	2013-12-11	86.7
<i>XMM-Newton</i>	0672420101	2011-10-11	41.7
<i>XMM-Newton</i>	0672420201	2011-10-13	51.3
<i>XMM-Newton</i>	0672420301	2011-10-15	43.4

The spectra of all regions are extracted from each XMM-Newton observation using the standard ESAS tools `mos-spectra`, `mos_back`, `pn-spectra` and `pn_back`. The XMM-Newton regions are first converted into observation and instrument specific detector coordinates; however, because of the many point sources and complex region geometries, the expression is far too long for the data subspace, therefore it is necessary to first turn them into region fits files for extraction.

All spectra from both Chandra and XMM-Newton were optimally binned using the method described in [Kaastra & Bleeker \(2016\)](#), and all astrophysical parameters were linked through all spectra for a joint fit. Unless otherwise specified, all spectra in this work were produced in a similar way. These regions were finally fit using SHERPA version 4.16.0 (from CIAO-4.16), using the XSPEC version 12.13.1e model library and AtomDB version 3.0.9.

2.3. MUSTANG2 Sunyaev-Zeldovich Observations

MACS J0717.5+3745 was observed by the 100-meter Green Bank Telescope (GBT) under project codes AGBT17A_340 and AGBT17B_266 (in semesters 2017A & 2017B, respectively) using the MUSTANG-2 instrument, a 215-element continuum bolometer array operating at 90 GHz ([Dicker et al. 2014](#)). The observations were conducted using Lissajous daisy scans with radii of 3' and 3'5 ([Romero et al. 2020, 2023a](#)). The data processing was identical to that in, for example, [Romero et al. \(2020\)](#). The resulting map, produced using the MUSTANG-2 pipeline, is shown in the lower left panel of Figure 6. The total integration time on target was 2.6 hours and the resulting map has a resolution of 10'', with an RMS noise level of $\sim 28 \mu\text{Jy/bm}$.

2.4. CLASH Weak Lensing Observations

In this study, we use ground-based weak-lensing data products from the CLASH program, as presented in [Umetsu et al. \(2014\)](#). These products are derived from deep *BVR_{Ci}z'* imaging with Subaru/Suprime-Cam, complemented by UV imaging from Megaprime/MegaCam and near-IR observations from WIRCAM on the Canada–France–Hawaii Telescope (see also [Medezinski et al. 2013](#)). For further details on data reduction and weak-lensing analysis, refer to [Umetsu et al. \(2014\)](#).

3. Background analysis

3.1. Chandra Stowed Instrument Background

The Chandra Stowed Background files are generated in a similar procedure as the blank-sky background files and were scaled by the data over background count ratio in the 10-12 keV energy

range. The Chandra instrumental background can be described as a mixture of various signal contributions across different energy bands. Specifically, cosmic rays hit the detectors from every direction and create a continuum emission. Additionally, the particle interactions can produce instrumental X-ray fluorescence lines from the various elements in and around the detector.

Of the available background datasets, the total stowed background merged exposure time was 2.91 Ms from the year 2000, 2.57 Ms from the year 2005, and 1.68 Ms for the year 2009. Spectra were extracted from the full field of view of each available year and were modelled following a similar process as described in [Siemiginowska et al. \(2010\)](#) for Chandra and [Mernier et al. \(2015\)](#) for XMM-Newton, with independent fits for each of the detectors. Special care was also taken regarding the Faint or Very Faint imaging modes, resulting in modified models that involve these different cases. The stowed background data was modelled in the 0.7 keV to 10 keV band for both the ACIS-I and ACIS-S detectors. The continuum emission is defined by a broken power-law for the Faint imaging submode and by a power-law in the Very Faint imaging submode, while all instrumental lines were modelled using Gaussians and frozen to their best fits. [Bartalucci et al. \(2014\)](#) noted that the shape of the particle background is fairly consistent, and only the normalizations in different epochs are changing from year to year; therefore, we refrain from including redundant information for all years, and give detailed results of the continuum emission and instrumental lines in Tab. 2. Elements corresponding to line energies used in our background model were documented in other work ([Bearden & Burr 1967](#); [Suzuki et al. 2021](#)). The line energies which did not exactly correspond to reported lines were marked in the table with '*', while the 2.6 keV line was marked with '**' as it was not previously mentioned in other reference material. This line in particular showed up only in the ACIS-I stowed backgrounds and is unlikely to be an instrumental line, rather some artifact of the response itself. It was included in the ACIS-I model as an empirical improvement for completeness. All Chandra spectral fits reported in this paper were performed in the 0.7 to 7.0 keV range.

3.2. XMM-Newton Instrumental Background

Similar to the Chandra Stowed Backgrounds, the XMM-Newton Filter Wheel Closed instrumental backgrounds can also be described as a mixture of various spectral contributions across different energy bands. Besides the 'hard particle' (HP), or quiescent particle background (QPB) components shared with Chandra, XMM-Newton cluster source observations can additionally suffer from a residual contribution from a 'soft-particle' (SP) component; remnants of the quiescent soft proton contamination, which may still pervade throughout the data despite having been excised from the observation during the GTI cleaning step. These 'soft-protons' are particles trapped in Earth's magnetosphere, which are accumulated and concentrated by the flight optics during the orbit cycle, affecting around 40% of all observation time.

The hard particle components were modelled using all currently available FWC data, corresponding to a total merged exposure time of around 4.77 Ms. Specifically, around 1.958 Ms of data from MOS1, 1.924 Ms of data from MOS2, and 0.8841 Ms of Extended Full-Frame pn data. Spectra were extracted from the full field of view of all available FWC observations, and modelled following a similar process as described in [Mernier et al. \(2015\)](#), also with independent fits for each of the detectors.

The FWC data were modelled in the 0.3 keV to 10 keV band for the MOS1 and MOS2 detectors and in the 0.4 keV to 10 keV

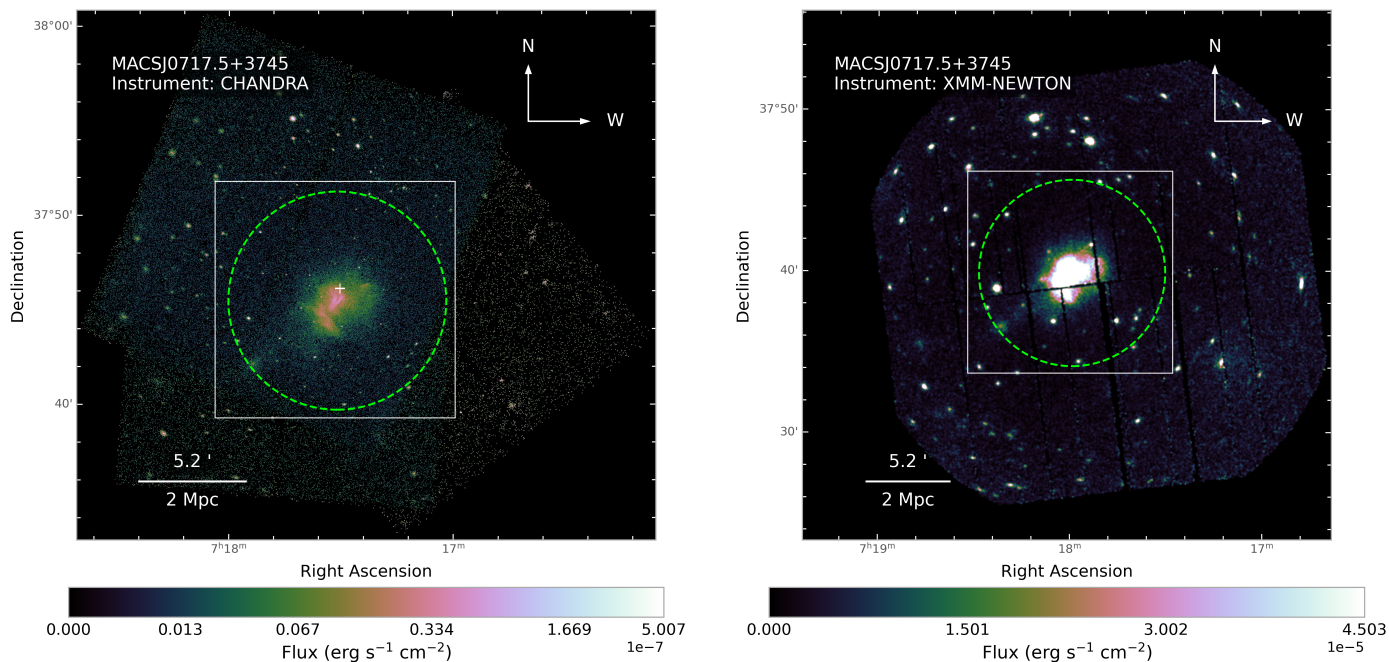


Fig. 1. Images of the full FOV of Chandra (left) and XMM-Newton (right) of MACS J0717.5+3745. The surface brightness excess to the west/south-west are several foreground structures in between us and the cluster. The green dashed circle indicates the approximate R_{200} of the cluster. Intensity scale is in flux per pixel (0.492×0.492 arcsec for Chandra, and 4.1×4.1 arcsec for XMM pn).

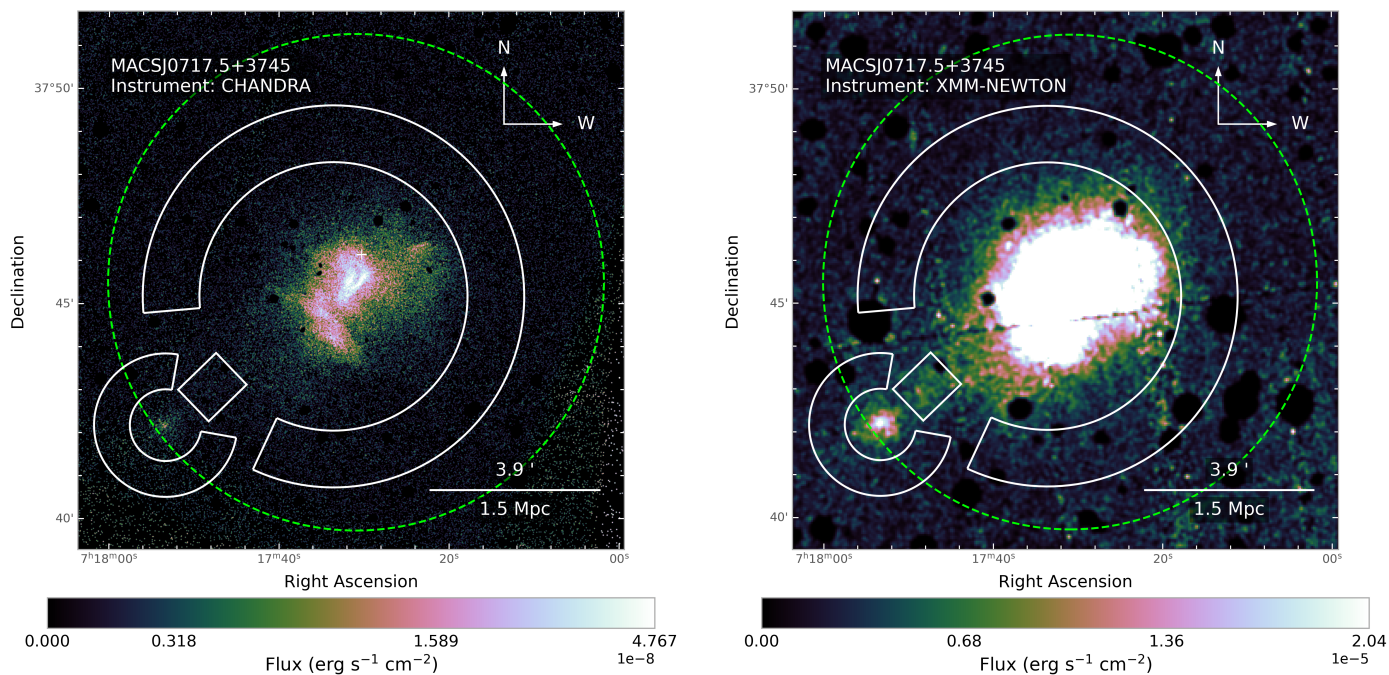


Fig. 2. The Chandra (left) and XMM-Newton (right) images of MACS J0717.5+3745, restricted to the same field of view as the Sunyaev-Zeldovich data and thermodynamical maps, visible as the box in Fig. 1. Intensity scale is in flux per pixel (0.492×0.492 arcsec for Chandra, and 4.1×4.1 arcsec for XMM pn). Part of the XMM-Newton image is over-saturated so that the filament structure is more visible. The white lines indicate the regions used for modelling the spectra of the outskirts of the cluster and the group together with the filament. The green dashed circle indicates the approximate R_{200} of the cluster.

range for pn. The continuum emission is fitted by a broken power-law, while all elemental lines were modelled using Gaussians described in Tab. 3. Because these HP components are noise contributions directly from the detectors and are unrelated to the mirrors, these instrumental background models are not convolved by the Ancillary Response File (ARF).

The residual SP components can be also be described as an ARF-unfolded power-law component with an index limited to a range between 0.1 and 1.4, which affects source spectra. However, the inclusion of the additional power-law did not contribute to an improvement in the background model fit statistics, indicating that the soft protons were fairly well treated in the data reduction.

Table 2. Summary of the ACIS-I and ACIS-S Stowed Background Data: Best-fit parameters of the continuum emission components and summary of instrumental lines, used as initial parameters for the automatic background fitting routine. Line energies with * indicate uncertainty in the Element/Type, represented by closest reported lines, ** indicates an undocumented line.

Best-fit Parameters of the Continuum Components				
Parameters	Faint (bkn-pow)		Very-Faint (pow)	
	ACIS-I	ACIS-S	ACIS-I	ACIS-S
Γ	2.386	2.386	0.349	0.349
E_{break} (keV)	0.692	0.692	-	-
$\Delta\Gamma$	0.418	0.418	-	-
norm	0.104	0.104	0.194	0.194

Summary of Instrumental Lines			
ACIS-I		ACIS-S	
Energy (keV)	Element	Energy (keV)	Element
0.529	-	-	-
1.490	Al $K\alpha$	1.490	Al $K\alpha$
1.786	Si $K\alpha$	1.786	Si $K\alpha$
2.141*	Au $M\alpha_1/M\alpha_2$	2.142*	Au $M\alpha_1/M\alpha_2$
2.6**	-	-	-
7.478	Ni $K\alpha$	7.478	Ni $K\alpha$
8.3*	Ni $K\beta$ /Au L_1	-	-
9.74*	Au $L\alpha_1/L\alpha_2$	9.740*	Au $L\alpha_1/L\alpha_2$
-	-	9.755*	Au $L\alpha_1/L\alpha_2$

To further check for any residual soft proton contamination, we compared the area-corrected count rates between the 'inside' and 'outside' regions of the Field of View (FOV) for each detector in each observation, shown in Tab. 4 (De Luca & Molendi 2004). All of the diagnostic values are under the lowest soft proton threshold of 1.15, indicating that none of the event lists are additionally contaminated by soft protons. As such, in this paper, the soft proton parameters were removed from the background model, which reduced the overall complexity. All XMM-Newton spectral fits reported in this paper were performed in the 0.45 to 7.0 keV range for MOS and 0.3 to 7.0 keV for pn.

3.3. The Astrophysical X-ray Background

With the instrumental backgrounds accounted for, special attention must be given to carefully model the astrophysical components of the background before we can accurately constrain any of the physical parameters of the cluster component of the signal. Especially in the faint signal-to-noise (S/N) and signal-to-background (S/b) regimes, such as cluster outskirts or filamentary structures, the parameters are all very sensitive, so any small changes to the instrumental background can affect the astrophysical background, which can both collectively bias the final results.

The Cosmic X-ray Background (CXB) includes the unresolved point sources, distant Active Galactic Nuclei (AGN) typi-

Table 3. Comprehensive summary of MOS1, MOS2, and pn Filter Wheel Closed Data including Hard Particle components and Instrumental Lines used as initial parameters for the automatic background fitting routine. (M1) or (M2) indicate EPIC MOS1 or MOS2 only.

Best-fit Parameters of the Hard Particle Components			
Parameters	MOS1	MOS2	pn
Γ	2.30	2.42	6.05
E_{break} (keV)	0.58	0.52	0.48
$\Delta\Gamma$	0.24	0.26	0.34
norm	4.02	4.34	0.12

Summary of Instrumental Lines			
MOS		pn	
Energy (keV)	Element	Energy (keV)	Element
-	-	0.363	-
0.521 ^(M1)	-	-	-
0.62	-	-	-
0.750	-	-	-
0.942 ^(M2)	-	0.958	-
1.489	Al $K\alpha$	1.479	Al $K\alpha$
1.746	Si $K\alpha$	-	-
2.146	Au $M\alpha$	2.100	Au $M\alpha$
5.410	Cr $K\alpha$	4.520	Ti $K\alpha$
5.900	Mn $K\alpha$	5.410	Cr $K\alpha$
6.400	Fe $K\alpha$	6.375	Fe $K\alpha$
7.100	Fe K	7.450	Ni $K\alpha$
7.480	Ni $K\alpha$	8.011	Cu $K\alpha$
8.100	Cu $K\alpha$	8.580	Zn $K\alpha$
8.640	Zn $K\alpha$	8.860	Cu $K\beta$
9.710	Au $L\alpha$	9.520	Zn $K\beta$

Table 4. Summary of the XMM-Newton F_{in}/F_{out} data, indicating the soft proton contamination ratio between the inside and outside the FOV of the CCDs. Based on the ratios, none of the detectors on any observation were contaminated by soft protons.

ObsID	F_{in}/F_{out} M1	F_{in}/F_{out} M2	F_{in}/F_{out} pn
0672420101	1.102 ± 0.027	1.036 ± 0.023	1.027 ± 0.023
0672420201	1.032 ± 0.024	1.037 ± 0.022	1.015 ± 0.021
0672420301	1.050 ± 0.026	1.035 ± 0.024	1.026 ± 0.023

cally modelled with a photoelectrically absorbed power-law with slope frozen at 1.41 and a free normalization (Hickox & Markevitch 2006). The Galactic foreground sources can be described as a combination of several plasmas in collisional ionisation equilibrium (apec). They include the Local Hot Bubble (LHB), the Galactic Halo (GH), and recently another component, interpreted as a super-virialized (SV) component of our Galactic Halo, sometimes referred to as the 'Galactic Corona'. The LHB is an ap-

proximately 0.1 keV plasma originating from a local supernova remnant that we are currently residing in. It can be effectively modelled using the ROSAT *All Sky Survey* (RASS) data with the support of the soft X-ray bands from Chandra and XMM-Newton. Additionally, our Galactic Halo and its supervirial component are described by photoelectrically absorbed (tbabs, wilms), thermal APEC plasma models (Wilms et al. 2000). For all of these local, foreground CXB components, the redshift was frozen to 0, the abundances frozen to solar, with the temperatures and normalizations free to fit. Unless otherwise stated, the 1.41 power law photon index was kept frozen. Meanwhile, the neutral hydrogen column density for the CXB and in all subsequent fits was frozen to $N_{\text{H}} = 8.36 \times 10^{20} \text{ cm}^{-2}$, corresponding to the sum of the atomic and molecular hydrogen column densities along the line of sight¹ (Kalberla et al. 2005; Willingale et al. 2013).

To constrain the local CXB parameters, we use a carefully constructed ‘blank field’ for our observations by using all available data outside of the cluster R_{200} , from both the Chandra and XMM-Newton data, as well as spectra from the ROSAT All Sky Survey. The ROSAT All Sky Survey spectrum was extracted from an annulus with radii 0.15 and 1 degrees around the cluster centre, similar to van Weeren et al. (2017). We use a fit range for ROSAT PSPC-C/B between 0.09 and 2.0 keV based on previous calibration database plots of on-axis effective area curves. Meanwhile, the Chandra and XMM-Newton observations utilized the entire FOV of the observations with most point sources and emission regions removed. Additionally, the Chandra data excluded bright edges and the XMM-Newton data also had approximately 1 arcminute from the edges of the observations removed, as can be seen in Fig. 3.

The best-fit parameters of the foreground components are often degenerate with each other. For this reason the LHB, GH, SV, and unresolved point sources were determined using generous priors with the Bayesian X-ray Analysis tool, which uses a nested sampling algorithm (UltraNest²) for Bayesian parameter estimation and model comparison, and is employed as a tool for faint S/N data within the AGN community (Buchner 2021; Buchner et al. 2014).

The top part of Tab. 5 shows the results of the different CXB components, with and without the inclusion of the ROSAT All Sky Survey data, using both a background subtracted and background modelled fits. Without the ROSAT data, the LHB temperature was fixed to 0.09 keV and a free normalization. Using all available data and the background models, the best-fit results using all 13 spectra gave a LHB temperature of 0.108 ± 0.002 keV, GH temperature of 0.156 ± 0.002 keV, and SV temperature of 0.697 ± 0.011 keV, with a SV normalization around 10% that of the GH, consistent with other studies.

4. Results

4.1. Cluster Spectra and Thermodynamical Maps

Once the CXB parameters are constrained, it is possible to more accurately constrain the cluster emission and, consequently, to create thermodynamical maps and trend-averaged maps of MACS J0717.5+3745 to better study and visualize the ICM physics and internal structures. Specifically, we used a modified version of the contour binning algorithm from Sanders (2006), which we first translated into Python from C++, and have released as `pycontbin`³. This contour binning algorithm creates

regions with a pre-selected S/N ratio while conserving the general contours of the data by grouping neighbouring pixels of similar surface brightness and yields statistically independent regions. The contour binning maps were derived from an exposure corrected XMM-Newton mosaic image, scaled to have the approximate number of counts per pixel as the sum of observations. The smallest bin in this map corresponds to a circle of around 10.6 arcseconds radius, around the size of the Point Spread Function (PSF) of XMM-Newton. Like the CXB region, all contour bin map regions were converted into polygons and were extracted with both Chandra and XMM-Newton, with the idea that the Chandra resolution could be exploited in the joint fitting procedure as a correction to the fit results in the cases where the complex polygon region geometries occasionally fall under the size of the XMM-Newton psf.

We again use the model for a plasma in collisional ionization equilibrium (apec) with photoelectric absorption (tbabs), but now with fixed values for the metallicity at 0.3 Solar and redshift at 0.5458. We additionally scale each region by its area in arcminute² using a model constant, so that we can simultaneously fit the large cxb region with each cluster spectra. The CXB parameters are first frozen to their best-fit values before fits are performed to constrain the cluster temperatures kT and normalizations $norm$. Finally, the ICM spectra abundances are thawed to constrain the metallicity parameter for each region. This fitting procedure is repeated for every bin and for every instrument independently before being performed on the combined data from all observatories and again for the combined data from all available instruments. Unless otherwise mentioned, this spectral fitting methodology applies to any other spectral analysis considered for the rest of the paper.

Thermodynamical maps were computed from a scaled, exposure-corrected XMM-Newton mosaic image, with S/N values of 120, 100, 70, and 50 (14400, 10000, 4900 and 2500 counts per bin, respectively). Regions from S/N 120 were extracted from XMM-Newton, and the other bins from only Chandra to make use of the better spatial resolution. To compute asymmetric errors, we resample the multivariate distribution of the parameters from the covariance matrix provided by the fit results 100000 times, using the median and the 16th and 84th percentiles of the resampled distribution for the 68% confidence intervals. Shown in Fig. 4 is the S/N 120 temperature map and S/N 100 density map, along with their combined S/N pressure and entropy maps, all of which had relative errors and propagated uncertainties lower than 20%. Combining the S/N 120 and 100 region maps yields a better-resolved gradient between map regions at the expense of having completely statistically independent bins. This is our favoured method for improving the map resolution without suffering from over-smoothing, as seen in other binning methods. We discuss the maps in more detail in Sec. 5.1.

The temperature kT was derived directly from the spectral modelling, while the electron density n_e was computed from a normalization parameter, $norm$, formally defined as

$$norm = \frac{10^{-14}}{4\pi(d_A(z+1))^2} \int n_e n_p dV, \quad (1)$$

where d_A is the angular diameter distance, z is the redshift, and $\int n_e n_p$ is the integrated cluster emissivity over the chosen volume of gas in the cluster. The electron density n_e and ion density n_p are related as $n_e = 1.18n_p$. The electron density is calculated under the simplified assumption of a constant line-of-sight depth of 1 Mpc. The electron pressure and entropy are then determined as $P_e = n_e kT$ and $K = kT n_e^{-2/3}$, respectively. Due to the nature

¹ <https://www.swift.ac.uk/analysis/nhtot/>

² <https://johannesbuchner.github.io/UltraNest/>

³ https://github.com/jpbreuer/contbin_python

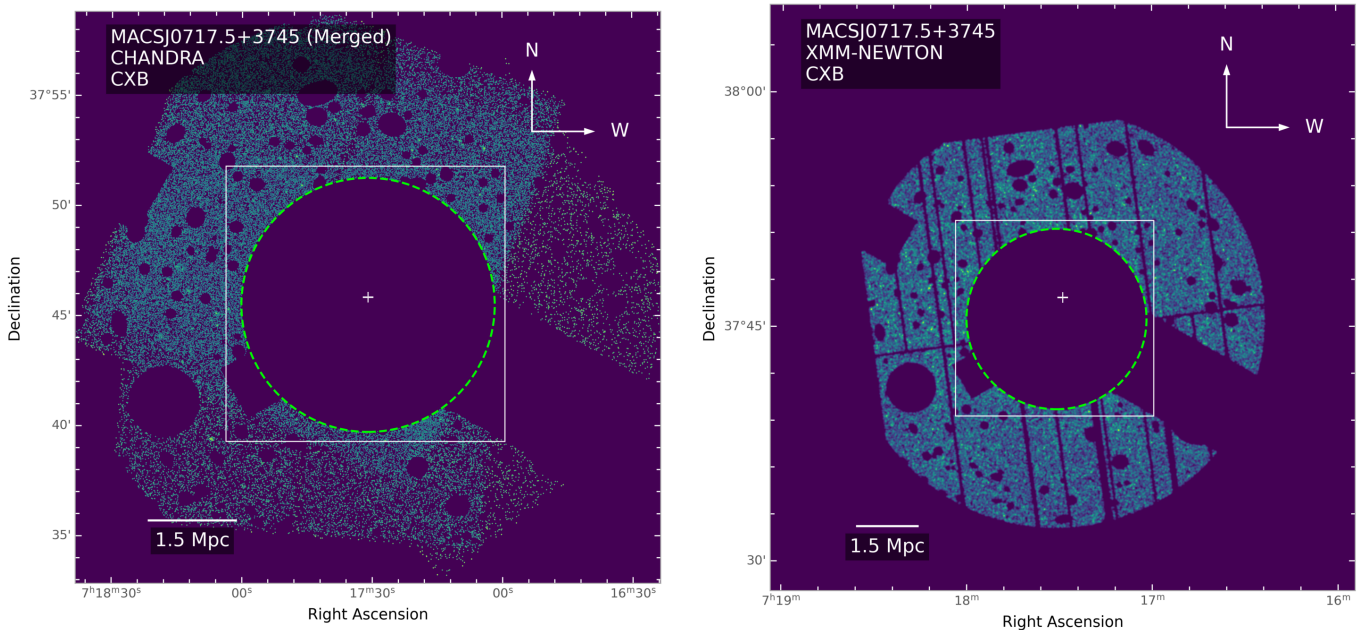


Fig. 3. The emission-free regions taken from the observations to fit the CXB components, with Chandra on the left, and XMM-Newton on the right. The box is the field of view used for Fig. 2 and the thermodynamical maps, corresponding to the total field of view of the Sunyaev Zeldovich data. The green dashed circle indicates the approximate R_{200} of the cluster. The excluded circles are removed sources, the large excluded box region to the west corresponds to removed foreground galaxies, and another smaller box removes the emission of the filamentary structure.

of merging systems, projection effects may bias the results due to potential asymmetries along the projected line of sight.

4.2. Azimuthal Trend-divided Maps

We additionally create trend-divided maps to enhance the small azimuthal variations present in the cluster seen in Fig. 5. We begin by calculating a centroid that is the average between the centre of the central contour bin (Bin 0), the position of the peak X-ray surface brightness pixel, and the best fitting results from a beta model fit to the cluster center. We then construct a scatter plot of the radial distribution for each physical quantity from the cluster centroid, and fit for the average trend using a function of the form,

$$f(r) = A(1 + (r/B)^2)^{-3C/2} (1 + (r/D)^2)^{-3E/2}, \quad (2)$$

where r is the radial distance from the centroid, and A, B, C, D, E are free parameters, following the method described in Ichinohe et al. (2015). Since we want to remove the general thermodynamical trends from the cluster, we do not use the full annuli, but instead restrict the radial distribution of physical quantities to the angles corresponding to the same region used to fit for the cluster outskirts. Trend-divided maps are then created for each physical quantity by calculating a residual for every bin, between the original value and the model-predicted value at the given radius.

4.3. Sunyaev-Zeldovich Estimates

Traditionally, the ICM has been studied by using X-ray observations; on the other hand, millimeter-wave astronomy provides an exceptional observational tool to directly probe gas pressure via the Sunyaev-Zeldovich (SZ) – Sunyaev & Zeldovich (1972) – effect (for a recent review, see Mroczkowski et al. 2019). The Sunyaev-Zeldovich effect is a spectral distortion in the frequency

spectrum of the cosmic microwave background (CMB) radiation due to inverse Compton scattering by a thermal plasma. In practice, it is commonly observed as either a decrement (or increment) in the CMB intensity at frequencies under (or over) 218 GHz along lines of sight through clusters of galaxies, with a linear dependence on the electron density (as opposed to X-ray observations which are dependent on electron density squared). The change in the effective CMB temperature is proportional to the Compton- y parameter, which depends on the Thomson scattering optical depth τ_e , and temperature of the hot electron gas T_e as,

$$y \equiv \int \frac{k_B T_e}{m_e c^2} d\tau_e = \int \frac{k_B T_e}{m_e c^2} n_e \sigma_T dl = \frac{\sigma_T}{m_e c^2} \int P_e dl \quad (3)$$

where the Thompson cross section, $P_e = n_e k_B T_e$ is the pressure due to the electrons, which integrates over the line of sight distance (Mroczkowski et al. 2019). There can additionally be another spectral distortion to the CMB spectrum due to the Doppler effect, known as the kinetic Sunyaev-Zeldovich effect, caused by the cluster bulk velocity along the line of sight on the scattered CMB photons, described by,

$$\frac{\Delta T_{SZ}}{T_{CMB}} = -\tau_e \frac{v_{\text{cluster}}}{c}. \quad (4)$$

Mroczkowski et al. (2012) and Sayers et al. (2013) both explored MACS J0717.5+3745 in the Sunyaev-Zeldovich, making the first discovery of a cluster system with a kinetic SZ component. Adam et al. (2017a) later made spatially resolved kinetic SZ maps of MACS J0717.5+3745 with the New IRAM KIDs Array (NIKA) on the IRAM 30m telescope, followed by a joint X-ray/SZ study of the projected gas temperature distribution (Adam et al. 2017b). Recently, Adam et al. (2024) also used NIKA data to probe the turbulent gas motions in MACS J0717.5+3745, finding a kinetic plus thermal pressure fraction $P_{\text{kin}}/P_{\text{kin+th}}$ of around 20% and an energy injection scale of around 800 kpc.

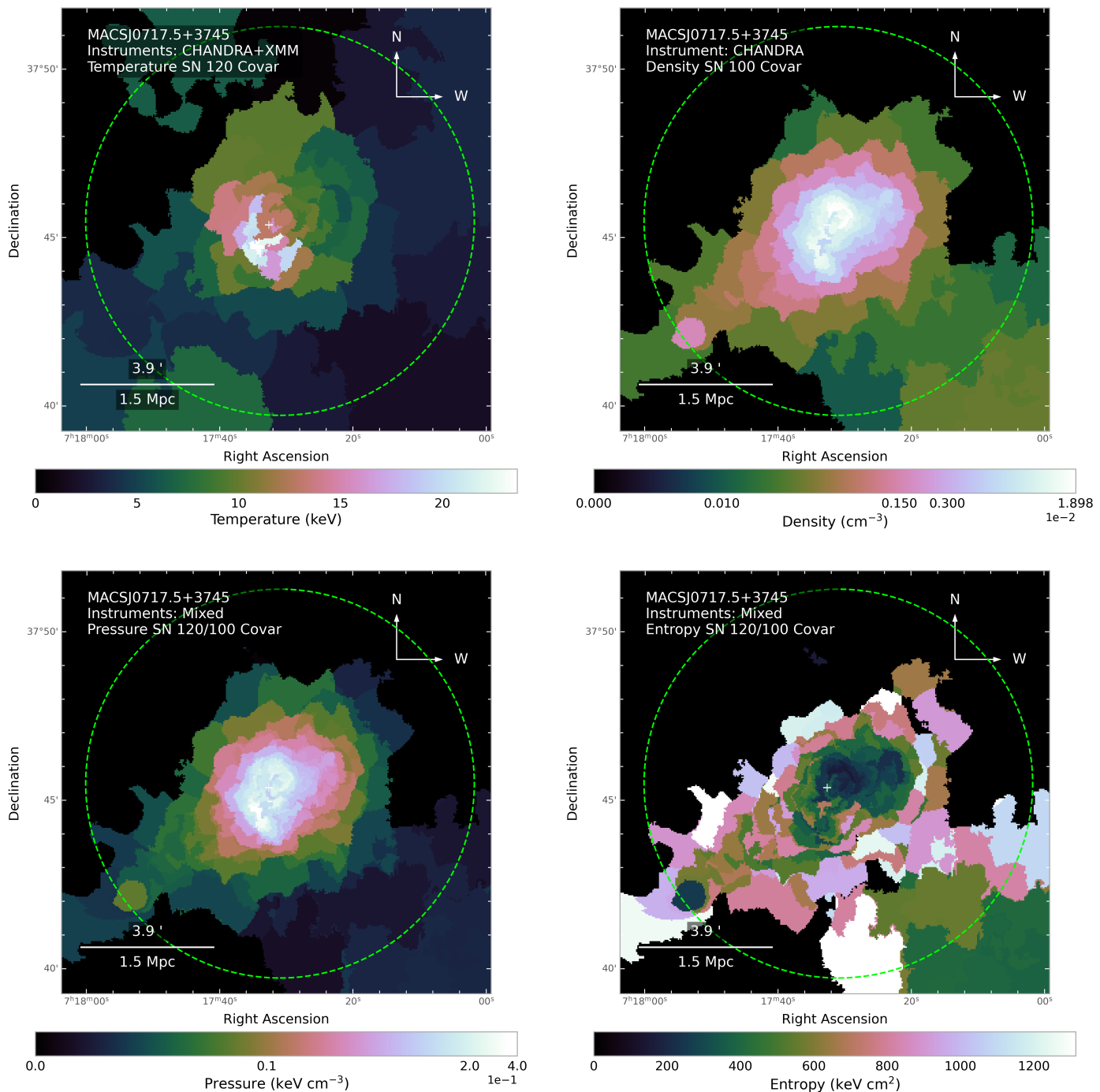


Fig. 4. Maps of temperature (*top left*), density (*top right*), pressure (*bottom left*), and entropy (*bottom right*) with corresponding units of keV, cm^{-3} , keVcm^{-3} , and keVcm^2 . The temperature and electron density maps were created using binning with a S/N of 120 (14400 counts) and 100 (10000 counts), respectively, while the pressure and entropy maps were produced using the results from the top two S/N maps. Density maps were derived from the normalization fits assuming a 1 Mpc projected line of sight depth. Spectral fits were made using data from both Chandra and XMM-Newton for the temperature, and only Chandra for the density, each using the CXB best fit results from ROSAT, Chandra, and XMM-Newton. Fits for these maps were performed using the most appropriate background model for each region according to the AIC.

Fig. 6 shows a comparison plot between a zoomed in view of the X-ray derived pressure and the trend-divided pressure maps (*top*), followed by Sunyaev-Zeldovich MUSTANG2 data and a weak lensing map derived from Subaru telescope data obtained by the CLASH program (*bottom*) (Umetsu et al. 2014). The white box corresponds to the FOV of the MUSTANG2 data, and is the same as the thermodynamical maps shown in Fig. 4 and Fig. 5, while the new smaller green box shows the zoomed in region in

the two top plots. The white contours are the radio images in van Weeren et al. (2017).

There is a relatively close agreement between the X-ray pressure peak and the SZ peak, with an offset corresponding to around 0.25 arcminutes, or around 100 kpc at this redshift, but this estimate is biased due to the resolution of the MUSTANG2 data and the size and shape of the corresponding bin from the X-ray pressure map. The present work does not explore pressure

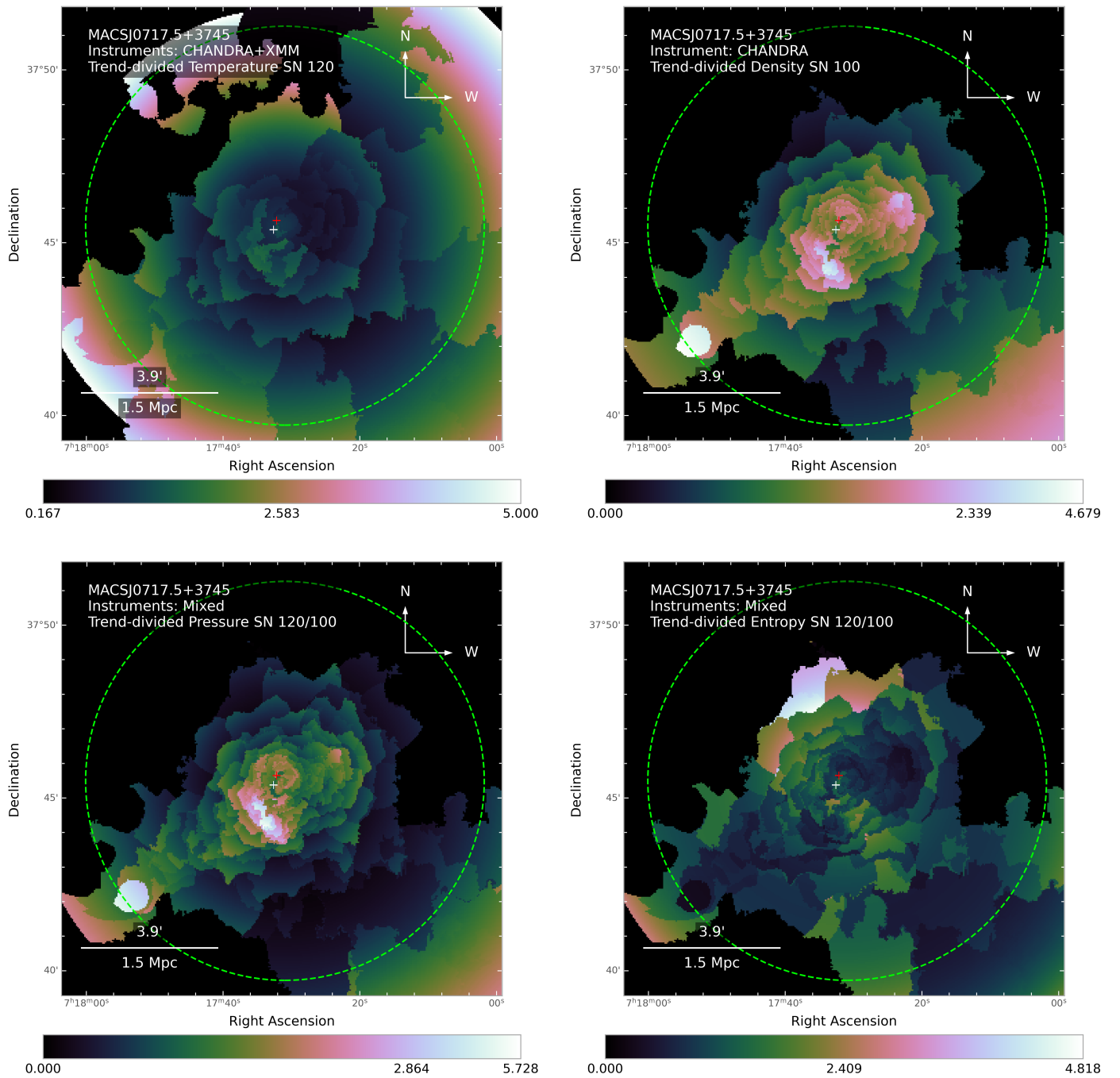


Fig. 5. Trend-divided maps of temperature (*top left*), density (*top right*), pressure (*bottom left*), and entropy (*bottom right*).

fluctuations (see [Khatri & Gaspari 2016](#); [Romero et al. 2023b, 2024](#)), but we note that deeper SZ observations with, for example, MUSTANG2, could improve upon the constraints for MACS J0717.5+3745 presented in [Adam et al. \(2024\)](#). Future MUSTANG2 observations could also provide a low frequency ballast point for constraining cluster temperatures via the relativistic correction to the thermal SZ, which, along with the known kinetic SZ shift, may explain the apparent discrepancy between X-ray and SZ results.

As can be seen from the trend-divided pressure map, there is also a clear offset between the radio relic emission and the X-ray pressure peak, likely due to the nature of the integrated X-ray emission and projection effects mentioned in [van Weeren et al. \(2017\)](#). In the CLASH map on the bottom right, it is possible to

note that the filamentary structure is also traced by gravitational lensing, and extends further to the south and south-east.

4.4. Spectroscopic Disentanglement of the Filament Signal

The spectroscopic fitting of the filamentary region was meticulously performed in several steps. We keep the standard assumption that it is a faint signal contaminated by instrumental backgrounds, as well as both astrophysical foreground and background signals; however, we extend the astrophysical description of the background to also include the local atmospheres of nearby systems. The filament lies between MACS J0717.5+3745 and a group to the southeast, inside their respective R_{200} emission areas, so to properly constrain the temperature and density of the

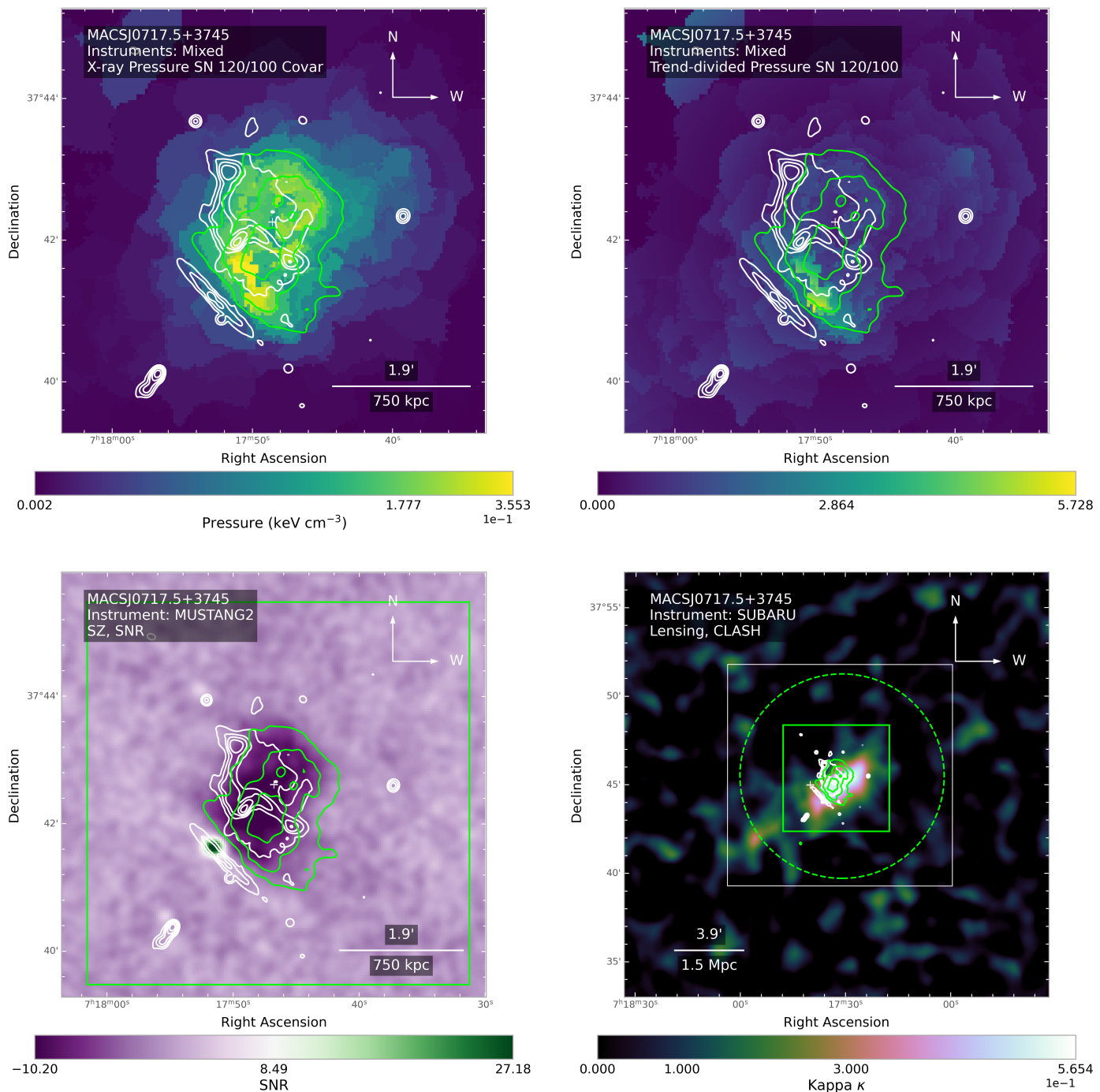


Fig. 6. Comparison plots between the X-ray pressure map (*top left*), the trend-divided X-ray pressure map (*top right*), followed by Sunyaev-Zeldovich MUSTANG2 data, displayed here as a SNR image (*bottom left*), next to a weak lensing map from the CLASH survey (*bottom right*) (Umetsu et al. 2014). The white contours are from the radio images seen in van Weeren et al. (2017), and the green contours corresponds to the MUSTANG2 data in the bottom left. The green box corresponds to the zoom-in region in the top left and top right figures, and the white box corresponds to the same FOV as the bottom left figure and the other thermodynamical maps. The full FOV of the MUSTANG2 data can be seen in Appendix Sec. C.

filament, it is first necessary to disentangle the different contributions to the complex signal.

To constrain the cluster and group-related contributions to the filament signal, large arc regions are extracted, approximately at the same radial distance at which the filament structure is displaced from the cluster and group centers, around R_{200} . These regions are then independently fit using a similar method described in Sec. 4.1, using CXB parameter constraints as determined from the optimal CXB fit, and then applying these posteriors as priors

to the subsequent fits. The fit results of the CXB + Cluster and CXB + Group regions are shown in the centre of Tab. 5.

As we do not know the exact multi-phase composition of the filamentary gas, we try to statistically disentangle the multi-phase nature of the region using Bayesian X-ray Analysis and model selection using the AIC and BIC criteria described in Appendix Sec. A. Tab. 6 shows the AIC and BIC values when comparing a combination of different spectral models that could effectively describe the filament region. To fit all of the various models, we

used only the CXB and filament spectra to fit the temperature and normalization of the filament data while all other parameters were frozen to their best fits. In these data were 3116 data points, and approximately 3114 degrees of freedom, so the AIC and BIC values are fairly close to each other.

We first compared a simple CXB + Filament (apex) model with a CXB + Filament (gadem) model, which applies a gaussian distribution of emission measure versus temperature to an apex model. Despite being often used to fit multi-phase plasmas, gadem was punished by the statistical measure for its extra complexity compared to apex, and was rejected as an option for the more complex model comparisons. We then proceeded to fit a CXB + Cluster + Filament model and a CXB + Group + Filament model, before finally fitting a rather complex model with CXB + Cluster + Group + Filament.

Based on the different criteria, all of the various apex models were close enough in their likelihoods with each other that they were not outright rejected and theoretically could each be effectively used to describe the data. That being said, the most complicated of the models, which contained the CXB + Cluster + Group + Filament, ended up with the best fit results, despite being punished for its extra complexity. Interesting to note is that the ‘second-best’ model according to the AIC is the CXB + Cluster + Filament, and not the expected CXB + Group + Filament model. This could be due to a bias in the region selection area, where we might have included more cluster emission than group emission, that the group atmosphere is not being effectively stripped by the filament accretion, that the filament region could be representative of a more simple ‘mixing’ zone between the two atmospheres, and there is a stronger cluster signal due to the difference in the size scales of the respective atmospheres, or due to other projection effects.

5. Discussion

5.1. Thermodynamical Maps

The temperature map on the top left of Fig. 4, shows an exceptionally hot cluster center, at around 24 ± 4 keV, with a temperature dropping to 9.8 ± 0.8 keV in the south and to 13 ± 3 keV in the north-northwest. North of the temperature peak, and slightly west of the radio contours (see Fig. 6 below), we find a ~ 20 keV elongated sub-structure; likewise, to the south and west of the peak, we see another ~ 20 keV sub-structure.

Farther out towards the outskirts, in the north-northeast direction we see a spatially large region with temperatures ~ 10 keV. To the west of MACS J0717.5+3745, after we pass the ~ 10 keV region, we reach a seemingly different plasma distribution with a 5 keV plasma surrounded by 6-7 keV plasma. Results approaching the R_{200} could potentially be biased by foreground structures and extended emissions to the west. In the south-southeast direction, we see a filamentary structure connecting the cluster with a group of galaxies. The filament temperature is reported in Tab. 5. In the map, the group itself has a temperature of 3.61 ± 0.17 keV, whereas the temperature reported in Tab. 5 gives the group R_{200} temperature. Based on previous lensing studies, it was determined that the filament continues farther out in this direction, even branching off into two separate filaments (Jauzac et al. 2018). Unfortunately, our X-ray data do not allow us to detect the X-ray emission associated with this part of the filamentary structure.

The measured density map traces the X-ray surface brightness image. We can also clearly see the density excess of the filament connecting the cluster and the group. Additionally, the density

map appears to trace the surface brightness excess at the ‘finger’ structure to the north-northwest described by van Weeren et al. (2017).

The large pressure discontinuities that we observe in the center of the cluster imply relatively strong shocks. Assuming the Rankine-Hugoniot jump condition for temperature, the temperature jumps of 13 ± 2 keV to 24 ± 4 keV (northwards), and 10 ± 1 keV to 21 ± 3 keV (southwards), would correspond to Mach numbers of $\mathcal{M} = 1.6 \pm 0.4$ and $\mathcal{M} = 1.9 \pm 0.3$, respectively. van Weeren et al. (2017) gives an estimate of the Mach number of the shock derived from the radio spectral index of $\mathcal{M} = 2.7$. The difference between our respective measurements of the Mach number can be attributed to projection effects in the observation, the complex geometry of the system, as well as our assumption of a 1 Mpc line of sight depth for the density map, which is most probably underestimating the strength of the Mach number. Our estimate of the shock Mach number was derived from the thermodynamical maps rather than from dedicated regions due to the complexity of the projected geometry.

Both the pressure peak of the X-ray map and Sunyaev-Zeldovich peak are offset from the gravitational lensing peaks, but are also approximately in the middle of the two largest merging structures. The pressure and SZ signal peaks are also cospatial with the radio contours. Previous discussions about the nature of these radio structures proposed a hypothesis that these are radio relics, as indicated by the pressure jumps nearby, which are seen at some peculiar projected geometry (van Weeren et al. 2017).

For a cluster in hydrostatic equilibrium, we expect to see an azimuthally symmetric and radially monotonously increasing entropy. Any departure from such a distribution is either due to the infall of subgroups hosting lower entropy material, uplift from the cluster centre due to AGN feedback, or shock heating. The entropy map shows that the group in the southeast has a relatively low entropy near the centre, which gradually increases with radius. The entropy of the X-ray bright bridge/filament appears lower than that of the surrounding ambient ICM at the same radius, which would be consistent with the potential infall of stripped material. At the position of the linear radio source, we see indications of an entropy discontinuity consistent with the presence of a shock front, where the lower entropy cluster centre increases at the boundary. This linear bar region to the south of the cluster centre is also cospatial with the temperature peak and associated X-ray shock features. Meanwhile, the characteristic ‘V’ shape, which is present in the cluster centre, seems to be associated with the colder region just north of the shock. The complex nature of the past subcluster merger activity and unknown geometry gives these shock discontinuities asymmetric and complex physical structures in projection.

Curious features also become apparent in the various trend-divided thermodynamical maps. In the trend-divided density map, besides the filamentary region to the south-west, three sub-clusters near the cluster centre show excess density, specifically the bar region associated with the shock front, the ‘V’ shaped emission region at the cluster centre, and the so-called ‘finger’ region to the north-west of the cluster. These regions also appear as overpressure regions associated with entropy decrements in the trend-divided pressure and entropy maps. New interesting features, now visible in the trend-divided entropy map, are two high entropy regions originating from the cluster centre and going to the northeast and southwest. Looking at the radio contours present in Fig. 6, the trend of this high entropy feature near the cluster centre seems to trace the radio shock reported by van Weeren et al. (2017), however, near the outskirts of the cluster, it

Table 5. The best-fit CXB, Cluster, Group, and Filament parameters from the joint fit using ROSAT, Chandra, and XMM-Newton data. The best fit was performed using *cstat* and includes all modelled Chandra and XMM-Newton instrumental backgrounds. Additional fits of the CXB, Cluster, Group, and Filament parameters excluding the ROSAT data were performed, with (*cstat*) and without (*wstat*) the instrumental background modelling.

Context	Source	Parameter	No ROSAT (<i>wstat</i>)	No ROSAT (<i>cstat</i>)	Best fit (<i>cstat</i>)
Cosmic X-ray Background	Local Hot Bubble	kT	0.09 (fixed)	0.09 (fixed)	0.108 ± 0.002
		Abundance	1 (fixed)	1 (fixed)	1 (fixed)
		Redshift	0 (fixed)	0 (fixed)	0 (fixed)
		norm	$(4.4^{+0.4}_{-0.2}) \times 10^{-6}$	$(4.3 \pm 0.2) \times 10^{-6}$	$(7.5 \pm 0.2) \times 10^{-7}$
	Galactic Halo	kT	$0.22^{+0.03}_{-0.01}$	$0.204^{+0.01}_{-0.004}$	0.156 ± 0.002
		Abundance	1 (fixed)	1 (fixed)	1 (fixed)
		Redshift	0 (fixed)	0 (fixed)	0 (fixed)
		norm	$(1.2 \pm 0.1) \times 10^{-6}$	$(1.2 \pm 0.1) \times 10^{-6}$	$(2.3^{+9.2}_{-0.1}) \times 10^{-6}$
	Supervirial Component	kT	$0.85^{+0.21}_{-0.02}$	$0.79^{+0.06}_{-0.02}$	$0.70^{+0.02}_{-0.01}$
		Abundance	1 (fixed)	1 (fixed)	1 (fixed)
		Redshift	0 (fixed)	0 (fixed)	0 (fixed)
		norm	$(2.6^{+0.2}_{-0.4}) \times 10^{-7}$	$(2.7^{+0.1}_{-0.3}) \times 10^{-7}$	$(3.4^{+2.3}_{-0.1}) \times 10^{-7}$
	Unresolved Point Sources	Photon Index	1.41 (fixed)	1.41 (fixed)	1.41 (fixed)
		norm	$(7.5 \pm 0.1) \times 10^{-7}$	$(7.9 \pm 0.1) \times 10^{-7}$	$(8.1 \pm 0.1) \times 10^{-07}$
Cluster	Cluster	kT	$5.2^{+0.5}_{-0.4}$	$5.7^{+0.5}_{-0.4}$	5.2 ± 0.4
		Abundance	0.3 (fixed)	0.3 (fixed)	0.3 (fixed)
		Redshift	0.5458 (fixed)	0.5458 (fixed)	0.5458 (fixed)
		norm	$(9.9 \pm 0.3) \times 10^{-06}$	$(1.000 \pm 0.02) \times 10^{-05}$	$(1.02 \pm 0.02) \times 10^{-05}$
Group	Group	kT	$3.6^{+0.7}_{-0.5}$	4.3 ± 0.60	$3.9^{+0.5}_{-0.4}$
		Abundance	0.3 (fixed)	0.3 (fixed)	0.3 (fixed)
		Redshift	0.5458 (fixed)	0.5458 (fixed)	0.5458 (fixed)
		norm	$(1.0 \pm 0.07) \times 10^{-05}$	$(1.08 \pm 0.06) \times 10^{-05}$	$(1.26 \pm 0.06) \times 10^{-05}$
Filament	Filament	kT	$2.6^{+0.4}_{-0.3}$	$2.8^{+0.4}_{-0.3}$	2.9 ± 0.4
		Abundance	0.3 (fixed)	0.3 (fixed)	0.3 (fixed)
		Redshift	0.5458 (fixed)	0.5458 (fixed)	0.5458 (fixed)
		norm	$(2.8 \pm 0.2) \times 10^{-05}$	$(2.7 \pm 0.2) \times 10^{-05}$	$(2.6 \pm 0.2) \times 10^{-05}$

Table 6. Comparison of BIC/AIC values for different potential filament models.

Model	BIC Value	AIC Value	AIC normalized, log ₁₀ (Z)
CXB + Filament (gadem)	4899.90	4881.77	-1.5
CXB + Filament (apec)	4893.75	4881.67	-0.7
CXB + Group (apec) + Filament (apec)	4893.71	4881.63	-0.4
CXB + Cluster (apec) + Filament (apec)	4893.08	4880.99	-0.3
CXB + Cluster (apec) + Group (apec) + Filament (apec)	4892.85	4880.76	0.0

may be associated with the foreground structures present in the west of the cluster system.

5.2. The Filament

The area of our selected rectangular filament region is 1.2 arcmin^2 , assuming a projected geometry, we calculate a volume of an elongated rectangular cuboid inclined near the line of sight based on the geometry proposed by Jauzac et al. (2012), where the assumed projected line of sight depth was determined to be $\sim (l/4000 \text{ kpc})$.

The filament temperature of $2.9^{+0.5}_{-0.3} \text{ keV}$ is lower than the cluster and the group temperatures at the same radius. The inferred filament density based on the assumed volume is $(1.60 \pm 0.05) \times 10^{-4} \text{ cm}^{-3}$. The filament has a lower entropy than the cluster and group outskirts. This can also be seen in the entropy map in the bottom right of Fig. 4, where a low entropy bridge is surrounded by a gas of higher entropy.

At the cluster redshift, the critical density of the Universe is $1.7 \times 10^{-29} \text{ g cm}^{-3}$. If we assume that the total baryon density is 0.044 of the critical density of the Universe and that the baryon mass fraction is 0.15 of the total mass density (Kirkman et al. 2003), we get an overdensity of our filament of 511 relative to the mean matter density of the Universe, and an overdensity of 150 relative to the critical density. Using the same volume, the baryonic mass of the filament is $\sim 4.2 \times 10^{12} M_{\odot}$. Assuming that the baryon fraction of the filament equals the mean cosmic value, its total mass would be $\sim 2.8 \times 10^{13} M_{\odot}$.

The inferred temperature of the filament region is relatively high compared to what would be expected of a WHIM filament. The ambiguity from the projection of the filament structure provides two potential hypotheses for this. Firstly, the increased temperature might be the result of compression as the cluster and group atmospheres interact with each other, or alternatively, the excess temperature could be also explained by shock heating from the WHIM accretion in the outskirts of the group atmosphere, similar to the proposed *external accretion shocks* (Ha et al. 2018; Gu et al. 2019). Lensing measurements of the filament structure, which reveal that it extends further to the southeast of the group, support this scenario. These types of shocks should, in theory, have high Mach numbers ($M \sim 10 - 100$), but have not yet been confirmed observationally since they are present in regions with very low X-ray surface brightness. Alternatively, the cooler component can be due to stripped low entropy gas from groups and galaxies seeding gas inhomogeneities in the direction of the large scale structure filament. A similar scenario was proposed for Abell 85 by Ichinohe et al. (2015).

Using the wide-field Subaru weak-lensing observations of Umetsu et al. (2014) to measure the mean surface mass density $\bar{\Sigma}$ within the filamentary region, we can provide an upper limit to the total mass of the filamentary structure. We note that the mass map shown in Fig. 6 was derived using Gaussian smoothing for visualization purposes (Umetsu et al. 2014), which is not suitable for accurate mass estimation. To this end, we employ the pixelized surface mass density map $\Sigma(\vec{\theta}_i)$ in the cluster field and its covariance matrix C_{ij} from Umetsu et al. (2018), derived from the combination of two-dimensional reduced shear and azimuthally averaged magnification-bias constraints using the cluster lensing mass inversion 2D (CLUMI-2D) code. Combining complementary shear and magnification measurements, this method reconstructs the underlying surface mass density field around the lens, effectively breaking the mass-sheet degeneracy (see Umetsu 2020, for a review of cluster weak lensing). The mass map $\Sigma(\vec{\theta}_i)$ covers a

field of $24 \times 24 \text{ arcmin}^2$ with $N_{\text{pix}} = 48 \times 48$ pixels centered on the cluster. We find $\bar{\Sigma} = (3.7 \pm 1.4) \times 10^{14} M_{\odot} \text{ Mpc}^{-2}$ using an optimal (minimum variance) estimator, $\bar{\Sigma} = [A^T C^{-1} A]^{-1} A^T C^{-1} \Sigma$ (Appendix C of Umetsu et al. 2015), where A is an $N_{\text{pix}} \times 1$ mapping matrix whose elements A_i are unity for those pixels lying inside the filamentary region and zero otherwise. The uncertainty for $\bar{\Sigma}$ is given by $\sigma(\bar{\Sigma}) = (A^T C^{-1} A)^{-1/2}$. This translates into a projected mass inside the filament region of $(6.8 \pm 2.7) \times 10^{13} M_{\odot}$. These large uncertainties are reasonable, given that the weak lensing-based mass reconstruction has a pixel scale of 0.5 arcmin ($\sim 190 \text{ kpc}$), which corresponds to only 7 pixels inside the filament region.

Taking these gas mass estimates ($4.2 \times 10^{12} M_{\odot}$) and the projected total mass measurements ($6.8 \pm 2.7 \times 10^{13} M_{\odot}$) at face-value, the gas mass fraction of the filament is 4–10%. This range is comparable to the upper limit of 9% determined for the filament in Abell 222/223 (Dietrich et al. 2012) and within the range of 5–10% inferred for the filament system around Abell 2744 (Eckert et al. 2015b).

6. Summary

MACS J0717.5+3745 is possibly one of the most dynamically active clusters in our Universe, making it also one of the most challenging galaxy clusters to study in the X-ray, owing to its geometric complexity, extremely high central temperature, as well as the many projected merging systems. Its rich radio morphology, X-ray substructures, and nearby filamentary structures have also paved the way for many interesting papers across different wavelengths.

In this paper, we presented results from deep X-ray observations of the merging cluster MACS J0717.5+3745 using a novel approach to dynamically model the instrumental and astrophysical backgrounds, as well as a new method to jointly fit Chandra, XMM-Newton, and ROSAT data from the entire FOV. We apply this method to constrain the CXB and instrumental background components, before fitting the respective regions, in an attempt to push the imaging and spectroscopic capabilities of these observatories to their limit. We provide new thermodynamical maps out to R_{200} using joint modelling of all available data, providing an order of magnitude improvement in spatial resolution with respect to the previous spectroscopic maps. We also present a novel use of statistical model comparison methods to disentangle the complex spectral emission from several overlapping X-ray components using Bayesian analysis tools, finding a new temperature component in the filamentary structure to the S-SE of the cluster. We also present a sensitive map of the Sunyaev-Zeldovich Effect decrement $10''$ resolution from MUSTANG-2 on the GBT.

To summarise the results:

- Thermodynamic maps produced from Chandra, XMM-Newton, and ROSAT data of MACS J0717.5+3745, using a new method for modelling both the astrophysical and instrumental backgrounds reveal a complicated ICM structure with several subsystems. The region south-southeast of the cluster center shows the presence of exceptionally hot $24 \pm 4 \text{ keV}$ gas and pressure discontinuities in the cluster core indicate the presence of shocks. To the south-southeast, we detect the X-ray emission of a large-scale structure filament connecting the cluster with a group.
- Trend-divided maps reveal that the localised density excess regions are related to the local overpressure regions, with a more complex entropy structure that appears approximately co-aligned to the spatial extent of the radio relic emission

reported by van Weeren et al. (2017). The filament structure and other subclusters are more clearly visible after removing the cluster average trend for each physical quantity.

- The temperature peak of 24 ± 4 keV is also the pressure peak of the cluster and is spatially offset from the Sunyaev-Zeldovich peaks by 0.25 arcmin, around 100 kpc. We report shock Mach numbers of $M = 1.6 \pm 0.4$ and $M = 1.9 \pm 0.3$, for shocks located approximately halfway between the two lensing mass peaks.
- Bayesian X-ray Analysis methods were used to disentangle different projected spectral signatures for the filament structure, with Akaike and Bayes criteria being used to select the most appropriate model to describe the various temperature components. The statistical measures indicate that the most complex model, involving CXB+Cluster+Group+Filament components is the best model to represent the filament structure. We report X-ray filament temperature of $2.9^{+0.5}_{-0.4}$ keV and density $1.60 \pm 0.05 \times 10^{-4} \text{ cm}^{-3}$, corresponding to an overdensity of the filament of 511 relative to the mean matter density of the Universe, and an overdensity of 150 relative to the critical density. We estimate the baryonic mass of the filament to be $\sim 4.2 \times 10^{12} M_{\odot}$, while its total projected weak lensing measured mass is $\sim 6.8 \pm 2.7 \times 10^{13} M_{\odot}$, indicating a hot baryon fraction of 4–10%.

Acknowledgements

Firstly, JPB would like to thank members of the *Chandra* CIAO/SHERPA help desk and the various calibration and instrument scientists for all of their help and advice. Special thanks is to be given to Nick Lee, for spending a year and over 120 emails helping me troubleshoot the development of the instrumental background fitting procedure, and for helping understand the many discovered bugs regarding the AREASCAL keywords and the background scaling in SHERPA. Special thanks is also to be given to the *XMM-Newton* helpdesk team and the SAS developers, for their time and patience helping address the many SAS-related problems with the development of the analysis pipeline. I would like to thank Dominique Eckert, Jelle de Plaa, and Jelle Kaastra, for several discussions and method-related motivation; Peter Boorman and Johannes Buchner for their help with using BXA; and Tomáš Plšek and Michal Zajaček for many helpful discussions. The scientific results reported in this article are based in part on data obtained from the Chandra Data Archive. This research has made use of software provided by the Chandra X-ray Center (CXC) in the application packages CIAO and SHERPA; as well as NASA's High Energy Astrophysics Software (HEASoft) packages XSPEC. The scientific results reported in this article are also based in part on observations obtained with XMM-Newton, an ESA science mission with instruments and contributions directly funded by ESA Member States and NASA. JPB and NW acknowledge the financial support of the GAČR EXPRO grant No. 21-13491X. The material is based upon work supported by NASA under award number 80GSFC21M0002. K.U. acknowledges support from the National Science and Technology Council of Taiwan (grant NSTC 112-2112-M-001-027-MY3) and the Academia Sinica Investigator Award (grant AS-IA-112-M04). L.D.M. has been supported by the French government, through the UCA^{J.E.D.I.} Investments in the Future project managed by the National Research Agency (ANR) with the reference number ANR-15-IDEX-01.

References

- Adam R., et al., 2017a, *A&A*, 598, A115
Adam R., et al., 2017b, *A&A*, 606, A64
Adam R., et al., 2024, *arXiv e-prints*, p. arXiv:2409.14804
Akaike H., 1974, *IEEE Transactions on Automatic Control*, 19, 716
Alvarez G. E., Randall S. W., Bourdin H., Jones C., Holley-Bockelmann K., 2018, *ApJ*, 858, 44
Bartalucci I., Mazzotta P., Bourdin H., Vikhlinin A., 2014, *A&A*, 566, A25
Bearden J. A., Burr A. F., 1967, *Reviews of Modern Physics*, 39, 125
Buchner J., 2021, *The Journal of Open Source Software*, 6, 3001
Buchner J., et al., 2014, *A&A*, 564, A125
Cash W., 1979, *ApJ*, 228, 939
Cen R., Ostriker J. P., 1999, *ApJ*, 514, 1
Cen R., Ostriker J. P., 2006, *ApJ*, 650, 560
Davé R., et al., 2001, *ApJ*, 552, 473
De Luca A., Molendi S., 2004, *A&A*, 419, 837
Dicker S. R., et al., 2014, in Holland W. S., Zmuidzinis J., eds, *Society of Photo-Optical Instrumentation Engineers (SPIE) Conference Series Vol. 9153, Millimeter, Submillimeter, and Far-Infrared Detectors and Instrumentation for Astronomy VII*. p. 91530J, doi:10.1117/12.2056455
Dietl J., Pacaud F., Reiprich T. H., Veronica A., Migkas K., Spinelli C., Dolag K., Seidel B., 2024, *arXiv e-prints*, p. arXiv:2401.17281
Dietrich J. P., Werner N., Clowe D., Finoguenov A., Kitching T., Miller L., Simionescu A., 2012, *Nature*, 487, 202
Ebeling H., Edge A. C., Henry J. P., 2001, *ApJ*, 553, 668
Ebeling H., Barrett E., Donovan D., 2004, *ApJ*, 609, L49
Eckert D., et al., 2015a, *Nature*, 528, 105
Eckert D., et al., 2015b, *Nature*, 528, 105
Ettori S., Molendi S., 2011, *Memorie della Societa Astronomica Italiana Supplementi*, 17, 47
Gu L., et al., 2019, *Nature Astronomy*, p. 347
Ha J.-H., Ryu D., Kang H., 2018, *ApJ*, 857, 26
Haider M., Steinhauser D., Vogelsberger M., Genel S., Springel V., Torrey P., Hernquist L., 2016, *MNRAS*, 457, 3024
Hickox R. C., Markevitch M., 2006, *ApJ*, 645, 95
Ichinohe Y., Werner N., Simionescu A., Allen S. W., Canning R. E. A., Ehlert S., Mernier F., Takahashi T., 2015, *MNRAS*, 448, 2971
Jauzac M., et al., 2012, *Monthly Notices of the Royal Astronomical Society*, 426, 3369
Jauzac M., et al., 2018, *MNRAS*, 481, 2901
Kaastra J. S., 2017, *A&A*, 605, A51
Kaastra J. S., Bleeker J. A. M., 2016, *A&A*, 587, A151
Kalberla P. M. W., Burton W. B., Hartmann D., Arnal E. M., Bajaja E., Morras R., Pöppel W. G. L., 2005, *A&A*, 440, 775
Katayama H., Takahashi I., Ikebe Y., Matsushita K., Freyberg M. J., 2004, *A&A*, 414, 767
Khatri R., Gaspari M., 2016, *MNRAS*, 463, 655
Kirkman D., Tytler D., Suzuki N., O'Meara J. M., Lubin D., 2003, *ApJS*, 149, 1
Madsen K. K., Beardmore A. P., Forster K., Guainazzi M., Marshall H. L., Miller E. D., Page K. L., Stuhlinger M., 2017, *AJ*, 153, 2
Medezinski E., et al., 2013, *ApJ*, 777, 43
Mernier F., de Plaa J., Lovisari L., Pinto C., Zhang Y. Y., Kaastra J. S., Werner N., Simionescu A., 2015, *A&A*, 575, A37
Mirakhor M. S., Walker S. A., Runge J., 2022, *MNRAS*, 509, 1109
Mitsuishi I., et al., 2012, *PASJ*, 64, 18
Mroczkowski T., et al., 2012, *ApJ*, 761, 47
Mroczkowski T., et al., 2019, *Space Sci. Rev.*, 215, 17
Nevalainen J., Markevitch M., Lumb D., 2005, *ApJ*, 629, 172
Nevalainen J., David L., Guainazzi M., 2010, *A&A*, 523, A22
Plucinsky P. P., Beardmore A. P., Foster A., Haberl F., Miller E. D., Pollock A. M. T., Sembay S., 2017, *A&A*, 597, A35
Reiprich T. H., et al., 2021, *A&A*, 647, A2
Romero C. E., et al., 2020, *ApJ*, 891, 90
Romero C. E., et al., 2023a, *ApJ*, 951, 41
Romero C. E., et al., 2023b, *ApJ*, 951, 41
Romero C. E., et al., 2024, *ApJ*, 970, 73
Sakellidou I., Ponman T. J., 2004, *MNRAS*, 351, 1439
Sanders J. S., 2006, *MNRAS*, 371, 829
Sato K., Kelley R. L., Takei Y., Tamura T., Yamasaki N. Y., Ohashi T., Gupta A., Galeazzi M., 2010, *PASJ*, 62, 1423
Sayers J., et al., 2013, *ApJ*, 778, 52
Schellenberger G., Reiprich T. H., Lovisari L., Nevalainen J., David L., 2015, *A&A*, 575, A30
Siemiginowska A., Burke D. J., Aldcroft T. L., Worrall D. M., Allen S., Bechtold J., Clarke T., Cheung C. C., 2010, *ApJ*, 722, 102
Simmonds C., Buchner J., Salvato M., Hsu L. T., Bauer F. E., 2018, *A&A*, 618, A66
Sugiura N., 1978, *Communications in Statistics - Theory and Methods*, 7, 13

- Sunyaev R. A., Zeldovich Y. B., 1972, *Comments on Astrophysics and Space Physics*, **4**, 173
- Suzuki H., Plucinsky P. P., Gaetz T. J., Bamba A., 2021, *A&A*, **655**, A116
- Umetsu K., 2020, *A&A Rev.*, **28**, 7
- Umetsu K., et al., 2014, *ApJ*, **795**, 163
- Umetsu K., et al., 2015, *ApJ*, **806**, 207
- Umetsu K., et al., 2018, *ApJ*, **860**, 104
- Veronica A., et al., 2022, *A&A*, **661**, A46
- Veronica A., et al., 2024, *A&A*, **681**, A108
- Wallbank A. N., Maughan B. J., Gastaldello F., Potter C., Wik D. R., 2022, *MNRAS*, **517**, 5594
- Werner N., Finoguenov A., Kaastra J. S., Simionescu A., Dietrich J. P., Vink J., Böhringer H., 2008, *A&A*, **482**, L29
- Willingale R., Starling R. L. C., Beardmore A. P., Tanvir N. R., O'Brien P. T., 2013, *MNRAS*, **431**, 394
- Wilms J., Allen A., McCray R., 2000, *ApJ*, **542**, 914
- van Weeren R. J., et al., 2016, *ApJ*, **817**, 98
- van Weeren R. J., et al., 2017, *ApJ*, **835**, 197

Appendix A: Automatic Background Fitting

Generally, due to accumulating ionizing doses from various orbit cycles, the quantum efficiency of CCD detectors slowly degrades over time, resulting in a change in the shape of the underlying continuum due to an increase of noise in different detector channels. The shape of the Chandra background continuum has historically been fairly stable (Bartalucci et al. 2014). The shape of the XMM-Newton background continuum however, has been observed to vary between 8% and 20% between quiet periods and maximum (Katayama et al. 2004), while also being sensitive to the cleaning method associated with the cleaning and removal of background flares (Nevalainen et al. 2005). Additionally, the relative strengths of the different X-ray fluorescence line emission components also differ across the detector area due to the shielding and other nearby electronics.

For the various, relatively small, spectral extraction regions, the background model derived from the full field-of-view of each detector is not the most appropriate model. However, for each region on the detector, the global, underlying spectral model created from the description of the full field-of-view is a good first-order approximation for the start of the automatic background fitting procedure.

The background contributions are scaled proportionally to the source and background region sizes in arcmin², by the exposure times between the source and backgrounds, and also by the high energy count rates in the 10 keV to 12 keV bands. Because the instrumental backgrounds originate from the detectors and are not dependent on the effective area of the optics, the instrumental background model should not be convolved by an Ancillary Response File (ARF); however, due to peculiarities with how models are set up in Sherpa, we instead build and convolve our model with a flat-ARF, which behaves the same as no ARF when convolved. There is a standing debate with regards to which is the correct response matrix to be used for the background since, arguably, a ‘correct’ response would need to be calibrated inside the spacecraft during flight for the detector background specifically, and a separate additional response would need to be done for the soft proton (and other particle) contributions. We explored the fit results when using the photon-derived response matrix calculated from standard spectral extraction tasks and compared it with the fit results when using a diagonal-response matrix, which effectively provides infinite instrument resolution for the background, and found that the results were comparable within a few per cent.

The background fitting procedure used in this paper works iteratively, carefully thawing and fitting model parameters in sequence, and becomes more fine-tuned as each model parameter is fit for the specific detector region. The background model is first normalized with a constant before fitting the continuum emission. The continuum is then fixed before the Gaussian line emissions are then subsequently thawed and fit, adjusting their shapes and relative ratios. Finally the normalization and continuum are then refit to slightly correct for the adjusted Gaussian lines.

The automatic background fitting routine initially defaults to fitting the full instrumental background first before fitting the source spectrum. By using robust instrumental background models, the typically difficult probes into faint signatures in poor S/N and S/b data regimes (such as cluster outskirts and filamentary structures close to R_{200}) can be exploited by leveraging the control over the systematics in the various backgrounds, preventing a loss of information through averaging or over smoothing of subtle spectral features which might be present in the data (Ettori & Molendi 2011). This background modelling procedure is addi-

tionally motivated by a well-known bias when subtracting backgrounds using ‘wstat’ statistics that treats every bin independently from one another (See Notebook 4). This ‘wstat’ bias is strongly affected by how spectra are binned, especially in low-resolution data, e.g., ROSAT. Modelling the background and using ‘cstat’ decreases the overall fit uncertainties when compared to ‘wstat’ because it treats all of the bins as continuous, even in the case of low or zero-count bins.

The caveat of this background fitting method, in particular, is that the background fitting procedure begins to fail when reaching very small regions with too few background counts. In other words, when the X-ray surface brightness is high (high S/N), the regions become small, which also increases the S/b and results in poor statistics. Coincidentally, this happens to be near the size of the PSF of each instrument. In these situations, the many parameters of the complex background model cannot be properly constrained. Therefore, the model becomes inappropriate with regard to the data quality of the background data. In these cases, we simplify the complex model to adjust to the data quality. We begin to do this by first removing the instrumental Gaussian lines so that we can fit a constant and the continuum. Then we try to also remove the continuum emission, and simply fit a constant model to the background. After each of these fits are performed, the reduced statistic, Akaike Information Criterion (AIC), and Bayes Information Criterion (BIC) are computed, and the most appropriate background model is selected for the dataset. For the very extreme cases, other background modelling methods and tools exist which could also be used; however, in this high S/b regime, a debate could be made about the need for a background model in the first place since the background can effectively be treated as noise (Buchner et al. 2014; Simmonds et al. 2018; Suzuki et al. 2021).

The AIC and the BIC both give us indicators for model selection based on the computed evidence (Akaike 1974; Sugiura 1978). The small-sample size corrected AIC and BIC are described, respectively, via,

$$AIC_c = 2k - 2 \ln(\mathcal{L}) + \frac{2k^2 + 2k}{n - k - 1}, \quad (\text{A.1})$$

$$BIC = k \ln(n) - 2 \ln(\mathcal{L}), \quad (\text{A.2})$$

where k is the degrees of freedom in the model, n is the number of data points, and \mathcal{L} is the maximized value of the likelihood function. The non-corrected AIC equation is the same as Eq. A.1 without the final term.

As evident by the two equations, the AIC and BIC both try to account for the goodness of fit between models, with a penalty given for the number of model parameters, where respectively, the AIC penalty is $2k$, versus the BIC penalty of $\ln(n)k$. Generally speaking, this punishes model complexity to prevent favouring models which overfit the data. These values can then be used to inform model selection; however, this is only applicable when comparing nested models relative to the same fitted data. The ‘cstat’ value is approximately equal to $-1/2 \ln(\mathcal{L})$ and has been shown to be a reliable estimator for model performance even with as few as 30 counts (Cash 1979; Kaastra 2017). We can then modify Eq. A.1 to give metrics for our background model selection.

Regardless of which background is chosen, the novelty of this tool is that the forward model is built completely from first principles, is intuitive, and is easily extendable, so new missions like XRISM and NewAthena will be able to benefit from

⁴ <https://giacomov.github.io/Bias-in-profile-poisson-likelihood/>

it as well. The background modelling tool is open source and will be released alongside a full pipeline for both Chandra and XMM-Newton, which handles the intermediate processing of the spectra⁵.

Appendix B: Instrumental Cross-calibration

There have been many studies exploring the cross-calibration between Chandra, XMM-Newton, and other X-ray observatories, motivated by the International Astronomical Consortium for High-Energy Calibration (IACHEC) using supernova remnants, quasars, and relaxed galaxy clusters (see Plucinsky et al. 2017, Section 6.1.2 for a detailed overview).

Using fluxes as a proxy, Nevalainen et al. (2010) found that the fluxes between Chandra ACIS and XMM-Newton pn had a large scatter; however, they were consistent within 2% in the soft band (0.5 - 2.0 keV) and that ACIS was, on average, 11% higher in the hard band (2.0 - 7.0 keV). Schellenberger et al. (2015), on the other hand, showed a difference in ACIS fluxes between 0-10% in the soft band and a 0-5% difference between ACIS and XMM-Newton MOS. A more recent study discusses an agreement on flux between ACIS and MOS below 3 keV, but the flux discrepancy rises to 10-15% above 4 keV (Madsen et al. 2017).

Regarding measured temperatures, previous studies have shown a 5-10% difference on the effective temperature between the MOS and pn detectors (Schellenberger et al. 2015). Chandra systematically has shown higher temperatures than XMM-Newton in the broad band, yet in another more recent study using Chandra and NuSTAR data, Wallbank et al. (2022) showed a 10.5% and a 15.7% temperature discrepancy between the instruments using the broad band (0.6 - 9.0 keV) and hard band (3.0 - 10.0 keV), respectively. An even more recent cross-calibration talk from the 2023 IACHEC meeting⁶ elaborated on this study further and discusses a complex relationship between the cross-calibrations between Chandra and XMM-Newton, using NuSTAR as a reference. This talk mentions that the temperature discrepancies between instruments increase with respect to measured temperatures, also noting a ~20% flux excess for XMM-Newton in the soft band. Furthermore, there is evidence that XMM-Newton agrees better with NuSTAR for hot clusters, while Chandra agrees better for cooler clusters.

We performed several independent tests to explore the cross-calibrations between the various instruments as part of the verification of our joint fitting methodology using the instrumental background models. We found a consistent, 12-17% cross-calibration related uncertainty between Chandra and XMM-Newton between the three different observations of MACS J0717.5+3745 and a 1-3% uncertainty between the MOS and pn detectors. To do this, we fit a circular region from the high S/N regime of MACS J0717.5+3745, shown as a red circle in Fig. 2, where there is an extremely hot ($\gtrsim 20$ keV) plasma emission, using a collisional ionisation equilibrium (apec) plasma model multiplied by a constant. We further explored the effect that the scaling of the instrumental backgrounds have on the fit results by scaling the Chandra backgrounds by the number of counts and also by scaling by the count-rate in the 10-12 keV band. We found that the temperatures were consistent between Chandra and XMM-Newton when the background was scaled by the ratio of the observation to background high-energy particle count rates, but that the normalizations were off by around 18%.

However, when the background is instead scaled by the ratio of the high-energy number of counts rather than by exposure time, the normalizations were within 5%, yet the temperatures were then off by around 22%.

Since we are jointly fitting all instruments from Chandra and XMM-Newton, the systematic uncertainties are accounted for in the averaged model fit between all instruments. Because MACS J0717.5+3745 is an exceptionally hot cluster, this means that in the high S/N regime where there are many counts, a joint fit will be more correctly weighted by the larger collecting area of XMM-Newton, while near the cooler cluster outskirts, this bias will be mitigated by the inclusion of the Chandra data. Despite our measured discrepancies between the different instruments, we found that our uncertainties fell within the previously reported limits from different IACHEC studies, so our new instrumental background modelling approach does not seem to be introducing any new biases to the measurements that were not already previously known or reported.

Appendix C: MUSTANG2 Full FOV Image

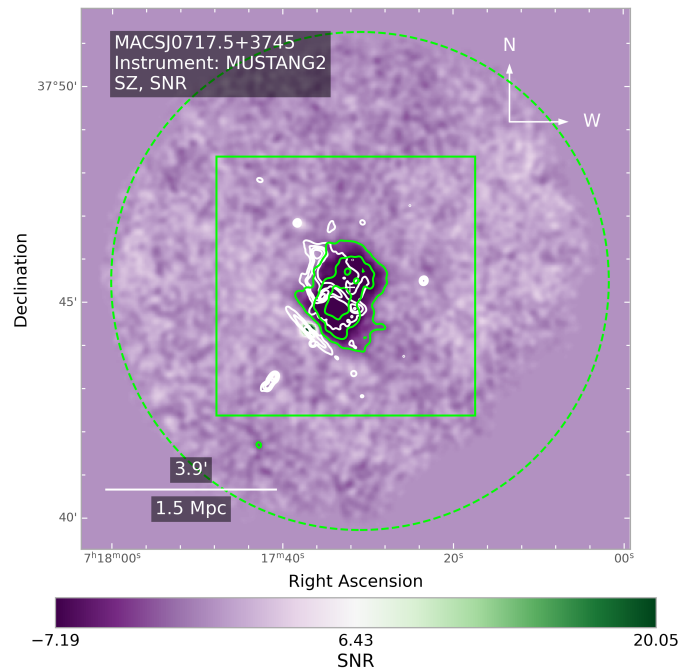


Fig. C.1. FOV of the signal to noise ratio of the MUSTANG2 data shown in Fig. 6. The FOV corresponds to the white box region shown throughout the paper, while the green box, and contours are the same as described in Fig. 6.

⁵ <https://github.com/jpbreuer>

⁶ <https://iachec.org/wp-content/presentations/2023/WikIACHEC2023.pdf>